Earth and Planetary Science Letters 323-324 (2012) 50–59

Contents lists available at SciVerse ScienceDirect

Earth and Planetary Science Letters

journal homepage: www.elsevier.com/locate/epsl

The influence of post-perovskite strength on the Earth's mantle thermal and chemical evolution

Henri Samuel [a,*], Nicola Tosi [b,c]

[a] Bayerisches Geoinstitut, Universität Bayreuth, Germany
[b] Department of Planetary Geodesy, Technical University Berlin, Germany
[c] Institute of Planetary Research, Department of Planetary Physics, German Aerospace Center (DLR), Berlin, Germany

ARTICLE INFO

Article history:
Received 31 October 2011
Received in revised form 13 January 2012
Accepted 21 January 2012
Available online xxxx

Editor: Y. Ricard

Keywords:
convective stirring
post-perovskite phase change
mantle heterogeneity
thermal evolution

ABSTRACT

We have investigated the influence of post-perovskite (ppv) viscosity on mantle convective dynamics and stirring efficiency, using numerical modeling and simple analytical theory.
Our results show that the strength of ppv has a dramatic influence on convective dynamics. The presence of a weak ppv enhances heat transfer across the bottom thermal boundary layer, resulting in higher temperatures, lower mantle viscosities and considerably larger convective velocities. This leads to a significant increase in stirring efficiencies with decreasing the ppv strength, by at least one order of magnitude.
In addition, using a simple parameterized convection evolution that includes the influence of ppv, coupled to a mixing model, we show that during the long term history of the Earth's mantle, the presence of ppv yields systematically hotter thermal evolution and more efficient convective stirring.
Such a strong effect of ppv strength on mantle stirring efficiency suggests that the influence of ppv phase must be considered when interpreting both geochemical and geophysical observations.

1. Introduction

Constraining the efficiency of stirring processes in the Earth's mantle is essential to the interpretation of surface geochemical record. In such a context, even the deepest parts of the Earth's mantle play an important role in influencing convective dynamics. The latter tend to homogenize geochemical heterogeneities via the repeated action of stretching and folding of mantle material (Hoffman and McKenzie, 1985; Ottino, 1989).

In the last years, a perovskite (pv) to post-perovskite (ppv) phase change occurring at deep mantle pressures was discovered by Murakami et al. (2004) and was later confirmed by additional experimental studies and *ab initio* calculations (Hirose et al., 2006; Oganov and Ono, 2004, 2005). In addition to the latent heat release, the presence of this exothermic phase change affects the physical properties of deep mantle material, such as density and compressibility (Boffa Ballaran et al., 2007; Komabayashi et al., 2008), thermal expansivity (Guignot et al., 2007), or thermal conductivity (Cheng et al., 2011; Ohta, 2010), therefore suggesting the potential impact of ppv on mantle convective heat transfer and dynamics.

For these reasons, several workers have studied the influence of ppv on mantle convection using theoretical and numerical approaches including various degrees of complexity (*e.g.*, compressibility, presence of compositional heterogeneities, variable heat transport properties or depth-dependent rheologies) (Buffet, 2007; Hernlund et al., 2005; Matyska and Yuen, 2006; Monnereau and Yuen, 2007, 2010; Nakagawa and Tackley, 2004, 2006; Tosi et al., 2009). A main result of these studies is that the presence of ppv leads to higher heat flux at the core–mantle boundary and increases mantle temperatures. The occurrence of ppv lenses is also suggested as likely cause of lowermost mantle heterogeneity inferred by seismic studies (Lay et al., 2006; van der Hilst et al., 2007).

Recent studies also point out the possibility of strong viscosity differences between the perovskite and the post-perovskite phases. The magnitude and sign, however, of such a pv–ppv viscosity contrast remains debated, with studies supporting the idea of a weaker ppv (Ammann et al., 2010; Hunt et al., 2009), while others suggest that a neutrally viscous or even a stronger ppv is possible (Karato, 2011). Investigations focusing on this pv–ppv rheological differences have found that the ppv rheology has a first order influence on mantle dynamics and thermal evolution (Čižkovà et al., 2010; Nakagawa and Tackley, 2011; Tosi et al., 2010), significantly amplifying the influences already observed for ppv with neutral viscosity.

The efficiency of convective stirring is directly related to the ability of material to deform (Ottino, 1989), therefore mantle viscous rheology plays a central role in convective stirring. The effect of mantle viscosity has been the focus of various studies (Tackley, 2007; van Keken et al., 2003 and references therein). For instance, the influence of vertical viscosity contrasts due to phase changes or spin transition was investigated by means of numerical experiments (Coltice, 2005;

* Corresponding author.
E-mail addresses: henri.samuel@uni-bayreuth.de (H. Samuel), nic.tosi@gmail.com (N. Tosi).

0012-821X/$ – see front matter © 2012 Elsevier B.V. All rights reserved.
doi:10.1016/j.epsl.2012.01.024

Farnetani and Samuel, 2003; Naliboff and Kellogg, 2006, 2007; van Keken and Ballentine, 1998). These studies concluded that an increase in viscosity yields smaller deformation, hence larger mixing times. Even a more gradual increase in viscosity due to lithostatic pressure effects leads qualitatively to a comparable behavior (Hunt and Kellogg, 2001). Similarly, local increase of viscosity due to compositional differences was found to reduce the efficiency of stirring (Manga, 1996; Merveilleux du Vignaux and Fleitout, 2002). Other forms of local variations of viscosity, either due to temperature-dependent (Christensen and Hofmann, 1994; Samuel and Farnetani, 2003), grain size-dependent (Solomatov and Reese, 2008), or to strain rate dependent rheologies (Ten et al., 1997) can also strongly affect the efficiency of stirring.

The relationship between mantle rheology and convective stirring illustrated by these studies naturally suggests that the presence of ppv with distinct rheological properties would have a significant impact on mantle stirring efficiency. However, this hypothesis has not been previously tested nor quantified.

Therefore, we focus here on the impact of ppv strength on mantle thermal evolution and convective stirring efficiency, using both numerical modeling and analytical theory.

The paper is organized as follows: Section 2 describes the numerical models and results used to investigate the effect of ppv on mantle stirring efficiency. Section 3 presents simple scaling laws for the heat fluxes and mantle temperatures in the presence of ppv with distinct rheology. A simple mixing model in good agreement with the measured stirring efficiency is derived in Section 4. In the last Section 5 preceding the discussion and conclusions, the scaling laws for heat flow and stirring efficiency are combined to test the impact of ppv on mantle convective stirring efficiency through its long-term history.

2. Numerical experiments

2.1. Governing equations and method

We use the finite-volume code YACC (*e.g.* Tosi et al., 2010) to solve the dimensionless conservation equations of mass, momentum and thermal energy in a Cartesian domain of aspect-ratio 1:3. In the frame of the Extended Boussinesq Approximation (*e.g.* King et al., 2010), they respectively read:

$$\partial_j v_j = 0, \tag{1}$$

$$-\partial_j p + \partial_j\left(\eta\left(\partial_j v_i + \partial_i v_j\right)\right) = Ra\left(\alpha T - \frac{Ra_{\mathrm{ppv}}}{Ra}\Gamma\right)\delta_{jz}, \tag{2}$$

$$\frac{DT}{Dt} = \partial^2_{jj}T + Di\ \alpha\ v_z(T+T_s) + \frac{Di}{Ra}\Phi + Di\ \frac{Ra_{\mathrm{ppv}}}{Ra}\frac{D\Gamma}{Dt}\gamma_{\mathrm{ppv}}(T+T_s), \tag{3}$$

where v_j are the components of the velocity, p is the dynamic pressure, η the viscosity, Ra the thermal Rayleigh number, Ra_{ppv} the phase Rayleigh number associated with the pv–ppv transition, α the thermal expansivity, T the temperature, T_s the surface temperature, Di the dissipation number, Φ the viscous dissipation, γ_{ppv} the Clapeyron slope of the pv–ppv transition and Γ the phase function. Following Christensen and Yuen (1985), the latter is defined as:

$$\Gamma = \frac{1}{2}\left\{1 + \tanh\left[\frac{z_d - 1 - \gamma_{\mathrm{ppv}}\left(T - T^0_{\mathrm{ppv}}\right)}{w}\right]\right\}, \tag{4}$$

where z_d is the depth, w the width of the phase transition and T^0_{ppv} the temperature intercept of the Clapeyron curve at the core–mantle boundary. Material constants and non-dimensional scaling are chosen as in Tosi et al. (2010). Table 1 lists the values and definitions of the non-dimensional numbers and of the parameters used for the pv–ppv transition.

Velocity boundaries are impermeable and free-slip. Temperature sidewalls are reflective, and horizontal boundaries are isothermal. Depending on the ppv viscosity, up to 800×400 grid points were used to discretize the spatial domain.

We measure the convective stirring efficiency using two Lagrangian methods: the first determines the mixing time associated with different wavelengths of heterogeneity following the approach of Ferrachat and Ricard (2001). The second determines the value of the maximum Finite Time Lyapunov Exponents (FTLE), λ^+, as described in Farnetani and Samuel (2003), and measures the rate at which heterogeneities are stretched by mantle motions. These methods were applied after each experiment had reached statistical steady state. The latter is considered to be reached whenever the average mantle temperature has reached a constant value (statistically speaking), which also corresponds to similar values of surface and bottom heat fluxes.

2.2. Viscosity and thermal expansivity

The dimensionless viscosity η is assumed to be Newtonian and dependent on dimensionless temperature and depth:

$$\eta(z_d, T) = \exp(-ET)\left[1 + 214.3 z_d \exp\left(-16.7(0.7 - z_d)^2\right)\right]. \tag{5}$$

For the temperature-dependent part (exponential term), we set $E = ln(10^3)$. This relatively low value prevents the formation of a stagnant-lid. The depth-dependent part (term in square brackets) implies a viscosity maximum in the mid lower mantle at a depth of around 1800 km (Tosi et al., 2010). This is consistent with geodynamic-based inversions of the geoid combined with mineral physics (Forte and Mitrovica, 2001; Ricard and Wuming, 1991; Steinberger and Calderwood, 2006) and several lower mantle constraints (Steinberger and Holme, 2008), as well as with molecular dynamics simulations of diffusion of MgO periclase (Ito and Toriumi, 2010).

The viscosity within the ppv-phase is:

$$\eta_{\mathrm{ppv}} = \Delta\eta_{\mathrm{ppv}}\ \eta(z_d, T), \tag{6}$$

where the viscosity contrast between pv and ppv phase, $\Delta\eta_{\mathrm{ppv}}$, was varied from 10^{-4} to 10 depending on the model.

In models where the depth-dependence of the thermal expansivity is taken into account, α varies with the dimensionless depth z_d as:

$$\alpha = \begin{cases} (1 + 0.78 z_d)^{-5} & \text{if } 0 \le z_d \le 0.23 \\ 0.44[1 + 0.35(z_d - 0.23)]^{-6.5} & \text{if } 0.23 < z_d \le 1. \end{cases} \tag{7}$$

Eq. (7) implies an overall decrease of α by about one order of magnitude throughout the mantle. The exponents 5 and 6.5 are the Anderson–Grüneisen parameters for the upper and lower mantles, respectively. These values are consistent with experimental measurements on olivine (Chopelas and Boehler, 1992) and perovskite (Katsura et al., 2009).

2.3. Results

Fig. 1 displays the temperature and velocity fields for four cases with depth-dependent thermal expansivity, at statistically steady state. Panel (a) corresponds to the reference case that has no ppv, while panels (b–d) display cases with decreasing values of ppv viscosity, starting from a stronger ppv ($\Delta\eta_{\mathrm{ppv}} = 10$, panel (b)) to weak ppv ($\Delta\eta_{\mathrm{ppv}} = 10^{-2}$, panel (d)). The presence of a strong ppv leads to colder mantle (Fig. 1b), and consequently thicker ppv patches.

Table 1
Non-dimensional numbers and parameters used for the pv–ppv transition. The subscript s refers to surface values. ρ indicates the reference density, κ the thermal diffusivity, C_p the heat capacity, g the gravity acceleration, h the mantle depth and ΔT the temperature drop across the mantle.

Definition	Description	Value
$Ra = \frac{\rho\alpha_s \Delta T h^3 g}{\eta_s \kappa_s}$	Surface thermal Rayleigh number	1.9×10^7
$Rb_{ppv} = \frac{\delta\rho_{ppv} h^3 g}{\eta_s \kappa_s}$	pv–ppv phase Rayleigh number	2.7×10^6
$Di = \frac{\alpha_s h g}{C_p}$	Surface dissipation number	0.68
T^0_{ppv}	Temperature intercept for pv–ppv transition	3600 K
γ_{ppv}	Clapeyron slope for pv–ppv transition (Tateno et al., 2009)	13 MPa K^{-1}
$\delta\rho_{ppv}$	Density contrast for pv–ppv transition (Oganov and Ono, 2004)	67.5 kg/m^3
w	Width of the pv–ppv transition	25 km

Conversely, mantle temperatures increase with decreasing the ppv strength, leading to thinner ppv patches (Fig. 1c–d). Although for all cases shown in Fig. 1 the pattern of convective currents is comparable, the magnitude of convective velocities increases with decreasing the ppv viscosity. This is the result of higher mantle temperatures associated with weaker ppv, which induce lower viscosities, and therefore higher convective vigor, in agreement with previous studies (Nakagawa and Tackley, 2011; Tosi et al., 2010).

These effects of ppv strength on mantle convection can be analyzed in more detail in Fig. 2. The presence of a weaker ppv facilitates the destabilization of the lower thermal boundary layer, which strongly enhances the heat flux (Fig. 2a). As a result of the increase in bottom heat transfer, the temperature rises significantly (Fig. 2b). Such a temperature increase leads to a decrease in mantle viscosity, which enhances the convective vigor, as illustrated in Fig. 2c, where the Root Mean Squared velocities significantly increase with decreasing $\Delta\eta_{ppv}$. Fig. 2d displays the distribution of the maximum Finite Time Lyapunov Exponents, λ^+, for cases corresponding to three values of $\Delta\eta_{ppv}$. All distributions are Gaussian, reflecting the fact that stirring is efficient. However, the case with strong ppv has the smallest λ^+ values, while the case with weak ppv has the largest λ^+ values. This indicates that the efficiency of convective stirring increases with decreasing the ppv strength. Similarly, the measured mixing times displayed in Fig. 3 show the same strong dependence on the ppv viscosity. This suggests that the stirring efficiency is related to the magnitude of convective velocities, as previously observed in various geodynamic contexts (Coltice and Schmalzl, 2006; Farnetani and Samuel, 2003; Samuel and Farnetani, 2003; Samuel et al., 2011). In addition, a case with no ppv is also shown in Fig. 3 (triangle), for which the mixing time is comparable to the case with a 'neutrally' viscous ppv (*i.e.*, $\Delta\eta_{ppv}=1$). This shows that other effects associated to the ppv phase transition (*e.g.*, changes in density or latent heat release) have a minor influence on mantle stirring efficiency compared to that of the ppv strength.

Most of the results displayed in Figs. 2 and 3 correspond to cases with variable thermal expansion. However, the same qualitative influence of the ppv strength is observed for cases with constant thermal expansion coefficient. Quantitatively, the influence of ppv is more pronounced for cases with variable thermal expansion, as illustrated in Fig. 2b and reported in Tosi et al. (2010).

3. Scaling relationships for the average mantle temperature

In order to provide more physical insights into the results described in the previous section, we consider the energetics of a Boussinesq fluid, convecting in a domain of thickness h, and volume $V=h^3$, in the infinite Prandtl number limit. The domain is heated from below and cooled from above with a temperature difference ΔT between the upper and lower surfaces (Fig. 4). The viscosity is Newtonian and depends on the dimensional temperature, T, as described in Eq. (5), ignoring the pressure dependence: $\eta=\eta_0 \exp(-E\ T/\Delta T)$.

Denoting ΔT_t and ΔT_b the temperature difference across the upper and lower thermal boundary layers, of respective thicknesses δ_t and δ_b, and k the thermal conductivity, the heat fluxes across the upper and lower surfaces are $Q_t=k\Delta T_t/\delta_t$ and $Q_b=k\Delta T_b/\delta_b$. The system is considered to have reached statistically steady state so that $Q=Q_t=Q_b$, yielding:

$$\frac{T_i}{\delta_t}=\frac{1-T_i}{\delta_b}, \tag{8}$$

where T_i is the equilibrium dimensionless internal temperature.

This domain is arbitrarily subdivided into three regions: an uppermost region delimited by the thickness of the upper thermal boundary layer δ_t, a central region representing the bulk of the mantle, and a lowermost region whose thickness corresponds to the average height of the post-perovskite h_b, with the assumption that it includes the lower thermal boundary layer thickness: $h_b>\delta_b$.

The energetics of mantle convection in the presence of post-perovskite can be considered by estimating the total amount of dissipated kinetic energy within the convective domain, $\Phi_{tot}=\int_V \sigma_{ij}\dot{\varepsilon}_{ij} dV$, with σ_{ij} and $\dot{\varepsilon}_{ij}$ the deviatoric stress and strain rate tensor components. We start with the momentum Eq. (2) recast in dimensional form and simplified by considering only the density changes due to temperature variations (*i.e.*, in the frame of the Boussinesq approximation):

$$-\nabla p+\nabla\cdot\sigma+\rho\alpha g T\delta_{jz}=0, \tag{9}$$

where ρ is now the reference mantle density, T is the temperature perturbation with respect to the average domain value, α is the (constant) thermal expansion coefficient, and g is the acceleration of gravity.

Following the approach of Chandrasekhar (1961) we take the scalar product of the above momentum equation with the dimensional velocity vector $\mathbf{U}=(U_x,U_y,U_z)$ and integrating over the whole domain yields after some rearrangement:

$$-\int_V \nabla\cdot(\mathbf{U}\ p)dV+\int_V p\nabla\cdot\mathbf{U}\ dV-\int_V \nabla\cdot(\sigma\cdot\mathbf{U})dV-\Phi_{tot} +\int_V \rho\,\alpha\,g\,T\,U_z\ dV=0. \tag{10}$$

Due to the incompressibility constraint (Eq. (1)) the second term in the above kinetic energy equation vanishes. Using the divergence theorem, the first and third terms are recast as surface integrals, yielding:

$$-\int_S(\mathbf{U}\ p)\cdot d\mathbf{S}-\int_S(\sigma\cdot\mathbf{U})\cdot d\mathbf{S}-\Phi_{tot}+\int_V \rho\alpha g T U_z\ dV=0. \tag{11}$$

In a closed, impermeable domain with free slip or rigid boundaries both surface integrals are equal to zero and we are left with:

$$\Phi_{tot}=\int_V \rho\alpha g T U_z\ dV. \tag{12}$$

Denoting C_p the specific heat at constant pressure and assuming that convection is fully developed within the domain, the conservation of energy requires that $\rho C_p U_z T\cong Q$. Thus, the total amount of dissipated kinetic energy (or viscous dissipation) is balanced by the total amount of mechanical work performed by convection (*i.e.*, the buoyancy flux):

$$\Phi_{tot}\cong\frac{Q\alpha g h^3}{C_p}. \tag{13}$$

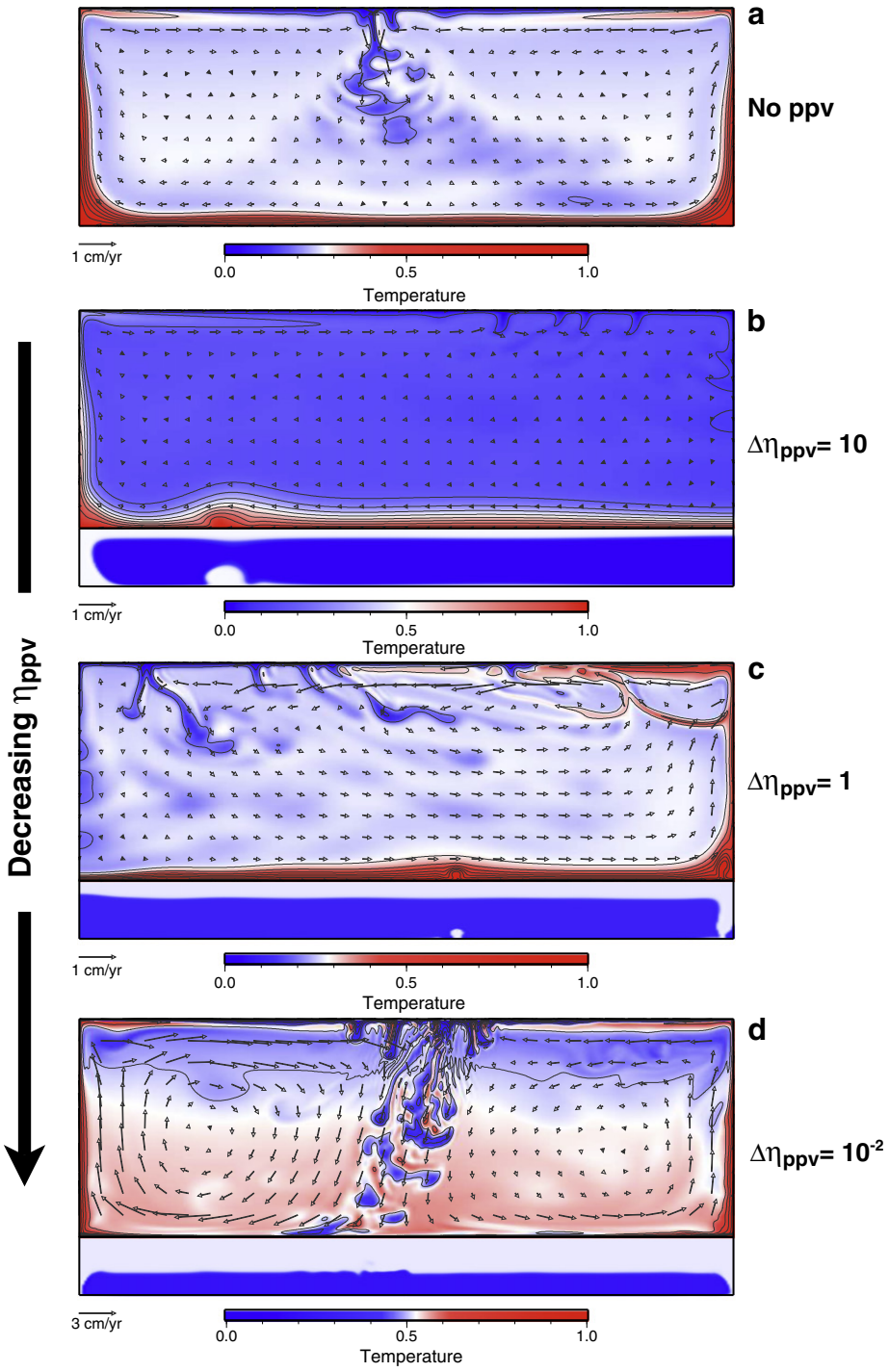

Fig. 1. Results of the numerical experiments. Dimensionless temperature and velocity fields for four experiments with depth-dependent thermal expansivity. (a) Case with no post-perovskite. (b–d) Cases including ppv phase change with $\Delta\eta_{ppv} = 10, 1, 0.01$, respectively. In panels b–d, the occurrence of the ppv phase is shown below the temperature field in a box comprising the lower 25% of the domain.

The total amount of viscous dissipation can be decomposed as the sum of the contribution of each of the three regions:

$$\Phi_{tot} = \int_{z=0}^{z=h_b} \bar{\Phi}\ dz + \int_{z=h_b}^{z=h-\delta_t} \bar{\Phi}\ dz + \int_{z=h-\delta_t}^{z=h} \bar{\Phi}\ dz = \Phi_b + \Phi_i + \Phi_t, \quad (14)$$

where the bars indicate horizontally averaged quantities.

Fig. 5a and b display horizontally averaged temperature and viscous dissipation profiles, respectively. In the absence of ppv phase change (green profiles), the viscous dissipation is largest in the top part of the upper thermal boundary layer. This maximum corresponds to the work done in a small volume $\delta_t^2\ h$ to bend the coldest (hence the strongest) part of the thermal boundary layer at a rate $\sim U_t/\delta_t$ before recycling slabs into the mantle, where U_t is the characteristic velocity in the top region. Therefore, the viscous dissipation in the top layer is (Conrad and Hager, 1999; Solomatov, 1995):

$$\Phi_t \sim \eta_0 \left(\frac{U_t}{\delta_t}\right)^2 \delta_t^2\ h. \quad (15)$$

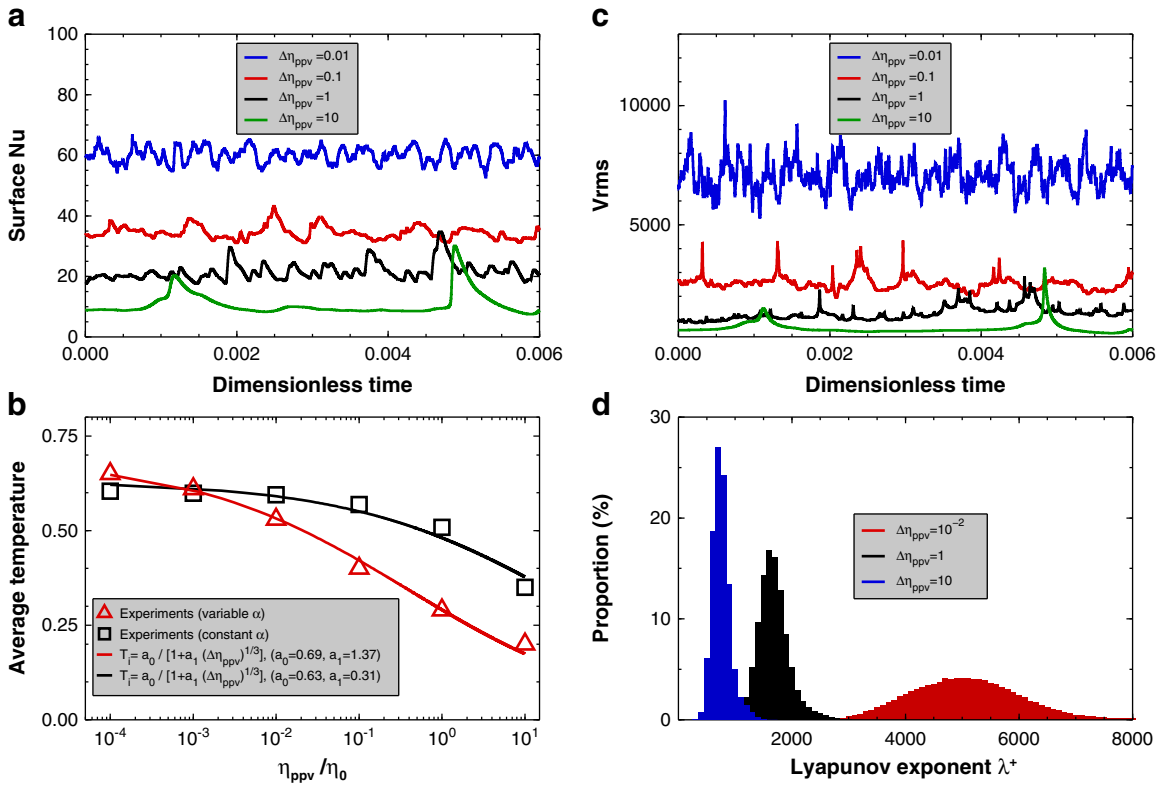

Fig. 2. Results of the numerical experiments including the ppv phase change, at statistically steady-state. (a) Time evolution of the surface Nusselt number for four values of $\Delta\eta_{ppv}=0.01, 0.1, 1.0, 10$. (b) Average dimensionless temperature, as a function of ppv strength $\Delta\eta_{ppv}$ for case with constant (black) or depth dependent (red) thermal expansion coefficient α. Each symbol represents a numerical experiment at statistically steady state. Curves are theoretical fits, using Eq. (27). (c) Time evolution of the RMS velocities for four values of $\Delta\eta_{ppv}=0.01, 0.1, 1.0, 10$. (d) Maximum Lyapunov exponent distributions for $\Delta\eta_{ppv}=0.01, 1.0, 10$. Panels a, c, and d correspond to cases with depth dependent thermal expansivity. (For interpretation of the references to color in this figure legend, the reader is referred to the web version of this article.)

On the contrary, in the lower thermal boundary layer the high temperatures yield low viscosities, and therefore small dissipation (Fig. 5a–b). However, if ppv is present and $\Delta\eta_{ppv}\neq 1$, the rheological contrast between pv and ppv leads to an increase in viscous dissipation within the ppv region, where the fluid is sheared at a rate $\sim(U_b/h_b)$ therefore the viscous dissipation in the ppv region of volume $h_b\ h^2$ and average viscosity $\eta_b=\Delta\eta_{ppv}\eta_0\ \exp(-E\ T_i)$ is:

$$\Phi_b \sim \eta_b \left(\frac{U_b}{h_b}\right)^2 h_b\ h^2. \tag{16}$$

The convective velocities in the top and bottom regions can be expressed using a boundary layer scaling:

$$U_t \sim \frac{\kappa\ h}{{\delta_t}^2}, \tag{17}$$

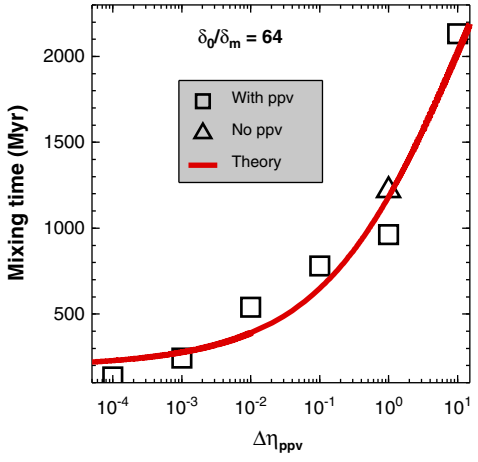

Fig. 3. Mixing time as a function of ppv strength $\Delta\eta_{ppv}$. Symbols are values measured experimentally. A case without ppv phase change is also shown (triangle). The red curve represents the chaotic mixing model, Eq. (29).

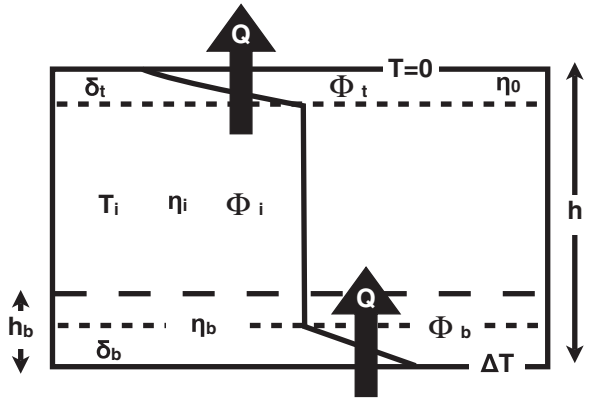

Fig. 4. Schematic representation of the convective domain at steady state: $Q_{top}=Q_{bottom}=Q$. See text for further definition of the symbols.

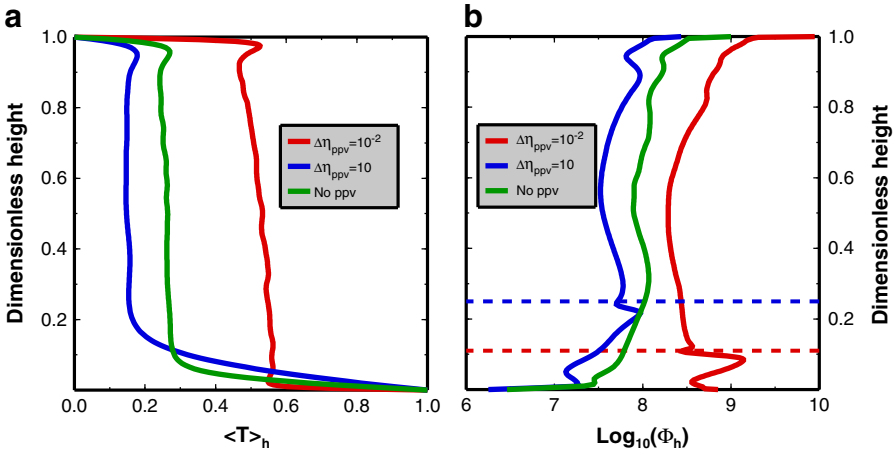

Fig. 5. Results from the numerical experiments. Horizontally averaged profiles for dimensionless temperature, $<T>_h$, (a) and viscous dissipation Φ_h (b) corresponding to cases with depth dependent thermal expansion, at statistically steady state. Three cases are shown: 'weak' ppv $\Delta\eta_{ppv}=0.01$ (red), 'strong' ppv $\Delta\eta_{ppv}=10$ (blue), and a case without ppv phase change (green). The horizontal dashed lines in (b) indicate the average thickness, h_b, of the ppv phase. (For interpretation of the references to color in this figure legend, the reader is referred to the web version of this article.)

$$U_b \sim \frac{\kappa\ h}{\delta_b{}^2}, \tag{18}$$

where $\kappa = k/(\rho C_p)$ is the thermal diffusivity, and ρ is the density.

As illustrated in Fig. 5b, the partitioning of Φ_{tot} into the different regions is not equal and may show a complex dependence on several parameters such as $\Delta\eta_{ppv}$, γ, E or α. However, regardless of these complexities, it is reasonable to assume that both Φ_t and Φ_b scale as Φ_{tot} (Jaupart and Mareschal, 2011). Therefore, using Eq. (13):

$$\Phi_t \sim \frac{Q\alpha g h^3}{C_p}, \tag{19}$$

and

$$\Phi_b \sim \frac{Q\alpha g h^3}{C_p}. \tag{20}$$

Combining Eqs. (8), (15), (17), and (19) yields an expression for the dimensionless thickness of the upper thermal boundary layer:

$$\frac{\delta_t}{h} \sim Ra_0^{-1/3}. \tag{21}$$

Where $Ra_0 = \rho\ g\ \alpha\Delta T h^3/(\eta_0\kappa)$ is the Rayleigh number based on the reference surface viscosity η_0. Note that for values of E larger than what we used in our numerical experiments, a more appropriate relationship for δ_t would be (Solomatov, 1995):

$$\frac{\delta_t}{h} \sim Ra_i^{-1/3}, \tag{22}$$

where $Ra_i = Ra_0\ \exp(-E\ T_i)$ is the Rayleigh number based on the viscosity at $T = T_i\ \Delta T$.

Similarly, the expression for the dimensionless thickness of the lower thermal boundary layer is obtained using Eqs. (8), (16), (18), and (20):

$$\frac{\delta_b}{h} \sim Ra_i^{-1/3}\left[\frac{h_b}{h}\frac{(1-T_i)}{\Delta\eta_{ppv}}\right]^{-1/3}. \tag{23}$$

In our numerical experiments, the dimensionless thickness of the ppv region is accurately described by the linear relationship:

$$\frac{h_b}{h} = 0.28(1-1.2\ T_i). \tag{24}$$

Re-writing Eq. (21), the average mantle temperature at (statistical) steady state T_i is:

$$T_i \sim \frac{1}{1+\frac{\delta_b}{\delta_t}}. \tag{25}$$

Using Eqs. (21), (23), and (24), the ratio of the thermal boundary layer thicknesses appearing in Eq. (25) is:

$$\frac{\delta_b}{\delta_t} \sim \left[\frac{(1-T_i)(1-1.2\ T_i)}{T_i\ \exp(E\ T_i)}\right]^{-1/3} \Delta\eta_{ppv}^{1/3}. \tag{26}$$

In the range $T_i = [0.2-0.65]$ covered in our experiments, the first term in the above equation varies around a mean by less than 15%. Therefore one can reasonably approximate the ratio of thermal boundary layer thicknesses as $\delta_b/\delta_t \sim \Delta\eta_{ppv}^{1/3}$. Thus, using Eq. (25), the expression for T_i becomes:

$$T_i \cong \frac{a_0}{1+a_1\Delta\eta_{ppv}^{\frac{1}{3}}}, \tag{27}$$

where the scaling constants a_0 and a_1 can be determined by fitting the results of the numerical experiments. Fig. 2 shows that Eq. (27) with

Table 2
Values of the parameters used for the thermal evolution model.

Reference parameter	Symbol	Value
Critical Rayleigh number	Ra_c	1000
Earth radius	R_t	6400 km
Earth core radius	R_c	3500 km
Temperature scale	ΔT	3000 K
Reference viscosity	η_0	10^{22} Pa s
Thermal diffusivity	κ	10^{-6} m^2/s
Thermal expansivity	α	10^{-5} K^{-1}
Density	ρ	4500 kg/m^3
Initial radioactive heat production	Q_0	90 TW
Radioactive decay time	τ_r	3×10^9 yr
Specific heat at constant pressure	C_p	1200 J kg^{-1} K^{-1}
Acceleration of gravity	g	10 m s^{-2}
Activation energy for the viscosity law	E	500 kJ/mol

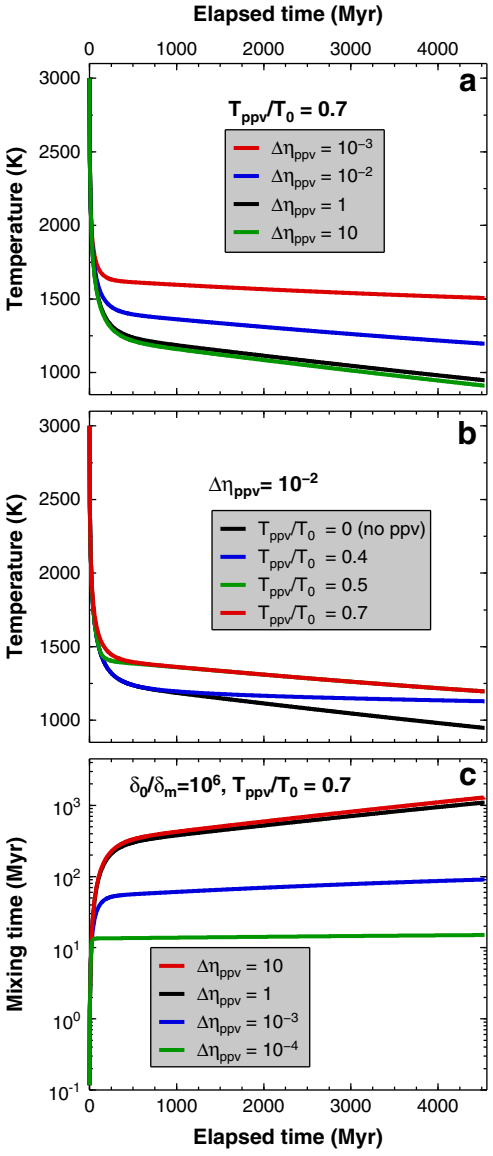

Fig. 6. Result from the parameterized convection model. Time evolution of whole mantle temperature (a–b) and convective mixing time (c) for different prescribed values of $\Delta\eta_{ppv}$ and T_{ppv}. (For interpretation of the references to color in this figure legend, the reader is referred to the web version of this article.)

$(a_0, a_1) = (0.63, 0.31)$ and $(a_0, a_1) = (0.69, 1.37)$ describes well the dependence of T_i on $\Delta\eta_{ppv}$ for cases with constant or variable thermal expansion coefficient, respectively.

4. Chaotic mixing model

To better interpret the mixing times measured in the numerical experiments we present a simple analytical model that follows closely the approach described in Samuel et al. (2011) and references therein.

We assume that the mechanical mixing is dominated by pure shear deformation. This assumption is reasonable for time dependent convective flows at Rayleigh numbers significantly larger than the critical onset value (Coltice, 2005; Farnetani and Samuel, 2003; Samuel et al., 2011). In this case a representative local velocity field in the (x,z) plane can be described by a stagnation/hyperbolic point flow of strain rate $\dot{\varepsilon}$: $\mathbf{U} = (\dot{\varepsilon}x, -\dot{\varepsilon}z)$ (Batchelor, 1967). Therefore, the convergence/shrinking occurs along the z direction and the size δ of a given heterogeneity close to the stagnation point shrinks as:

$$\frac{d\delta}{dt} = U_z(\delta) = -\dot{\varepsilon}\delta. \tag{28}$$

The strain rate $\dot{\varepsilon}$ is assumed to be related to the convective velocities as: $\dot{\varepsilon} \sim [Ra_0 \exp(E\ T_i)]^{2/3}$.

Integration of Eq. (28) with the assumption that $\dot{\varepsilon}$ remains constant yields the expression for the scale dependent mixing time τ (given in Myrs) defined as the time necessary for a heterogeneity of initial size δ_0, undergoing mechanical stirring, to be reduced to a given size δ_m:

$$\tau = c \ln\left(\frac{\delta_0}{\delta_m}\right) [Ra_0 \exp(E\ T_i)]^{-2/3}, \tag{29}$$

where the proportionality constant $c = 1.2 \times 10^8$ Myr was determined by least square fitting of the numerical experiments (Fig. 3).

Using Eq. (27) with the above expression, the predicted mixing time as a function of $\Delta\eta_{ppv}$ is in good agreement with the experimental results (Fig. 3). This confirms the interpretation of the numerical experiments presented in Section 2.3.

5. Simple cooling model with post-perovskite

Eq. (29) can be used to predict the mixing times as a function of the ppv strength for a given convective vigor which, in reality, is a function of time t. Therefore, to test the influence of ppv on stirring efficiency over the long-term evolution of the Earth's mantle, it is useful to consider a more realistic thermal history. Such a task can be performed using parameterized convection models (Davies, 1980; Schubert et al., 1980) that rely on a simple energy balance to describe the evolution of the average temperature T over the whole mantle $V = 4\pi(R_t^3 - R_c^3)/3$ (*i.e.*, corresponding to the spherical shell bounded by the Earth's mantle outer and inner radii, R_t and R_c, respectively):

$$\rho V C_p \ \frac{dT}{dt} = S_b \ Q_b - S_t \ Q_t + Q_i, \tag{30}$$

where C_p and ρ are the mantle density and specific heat, $S_t = 4\pi R_t^2$ and Q_t are the top surface and heat fluxes, $S_b = 4\pi R_c^2$ and Q_b their bottom counterparts. Q_i is the total amount of internal heat due to the disintegration of radionuclides (U, Th, K), and decays with time according to:

$$Q_i = Q_0 \ \exp\left(-\frac{t}{\tau_r}\right), \tag{31}$$

where $\tau_r = 3 \times 10^9$ yr is the decay time, and $Q_0 = 90$ TW is the initial total amount of radioactive heat production.

The surface and bottom heat fluxes Q_t and Q_b are calculated using Eqs. (22) and (23), respectively, assuming a proportionality constant equal to the inverse of the critical Rayleigh number Ra_c:

$$\delta_t = h\left(\frac{Ra_0}{Ra_c}\right)^{-1/3}, \tag{32}$$

and

$$\delta_b = h\left(\frac{Ra_0}{Ra_c}\right)^{-1/3} \exp\left(\frac{E\ T}{3\Delta T}\right) \left[\frac{h_b}{h}\frac{(1-T)}{\Delta T}\frac{\eta_0}{\eta_b}\right]^{-1/3}, \tag{33}$$

where $h = R_t - R_c$. The dimensionless viscosity in the bottom region is described by:

$$\frac{\eta_b}{\eta_0} = 1 + \frac{1}{2}\left[1 + \tanh\left(100\frac{T_{ppv} - T}{\Delta T}\right)\right]\left(\Delta\eta_{ppv} - 1\right), \tag{34}$$

where T_{ppv} is the temperature at which the pv–ppv transition occurs (*i.e.*, in this 1D model where no information about the temperature dependence with depth is available, T_{ppv} is analogous to γ). For simplicity we assume a constant ppv thickness $h_b = 0.05h$. Although our numerical experiments suggest a linear dependence of h_b with mantle temperature T (Eq. (24)), this simplification does not affect significantly the resulting thermal evolutions.

Table 2 lists the values of parameters used in Eq. (30). The latter is integrated forward in time for 4.5 Byr, using a fourth-order Runge–Kutta method, with the initial condition $T(t=0) = T_0 = \Delta T = 3000$ K.

Fig. 6 displays the results of the parameterized model. The presence of weak ppv enhances the basal heating, resulting in hotter mantles. Due to the temperature dependence of viscosity, the cooling is more efficient during the early history (Fig. 6a). During this short time period, mantle temperatures decrease below T_{ppv}, the threshold at which the ppv occurs. The early appearance of ppv with different viscosities triggers the development of temperature differences between the four thermal evolutions displayed in Fig. 6a. These differences grow with time, however at a decaying rate. The cases with the weakest ppv have developed temperatures that are about 250 K hotter than the case without ppv. Conversely, stronger ppv results in colder mantle. However, in this case the effect on the thermal evolution is much less pronounced (compare the green and the black curves in Fig. 6a).

To investigate the influence of T_{ppv} on the thermal evolution, cases with identical values of $\Delta\eta_{ppv} = 0.01$ (weak ppv), but with different values of T_{ppv} were considered and displayed in Fig. 6b. As expected, the reference case with no ppv has the coldest thermal history. On the contrary, the case with an early ppv appearance (*i.e.*, highest T_{ppv}) has the hottest thermal history. An intermediate case with a lower value of $T_{ppv} = 0.5$ (hence, a later ppv appearance) rapidly converges toward the hottest thermal evolution. This typical behavior is also observed for thermal evolutions without ppv starting with different initial temperatures. The non-linear feedback due to the temperature-dependent viscosity yields a faster cooling for cases with hotter mantles, resulting in similar thermal histories even for models that start with a different initial condition. However, for a smaller value of the pv–ppv transition temperature $T_{ppv} = 0.4$ (green curve), the appearance of ppv occurs about 2 Byr after the initial condition. In that case, although the thermal evolution also bifurcates toward hotter temperatures, the convergence toward the hottest thermal history (red curve) is slower. Consequently, the final temperature at $t = 4.5$ Byr remains significantly colder than the hottest cases (red and green curves). Therefore, the influence of ppv on the thermal evolution strongly depends on the value of T_{ppv} that determines how early ppv appears during mantle thermal history. In the case of an early appearance, the presence of weak ppv leads to a significantly hotter mantle for a large time period.

As seen in the numerical experiments (Figs. 1 and 2), such differences in thermal evolutions should result in differences in convective velocities, hence in stirring efficiencies. Using Eq. (29) together with Eq. (30), one can calculate the time evolution of the instantaneous mixing time τ at a given wavelength of heterogeneity, chosen here to be 10^{-6}. In other words τ represents the time necessary for convective motions to reduce the size of a passive heterogeneity by a factor 10^6. This would correspond for instance to the time necessary to reduce the thickness of a 10 km slab down to centimeter scale, at which solid-state diffusion becomes significant. Fig. 6c displays the result for cases with strong, neutral or weak ppv. As required by Eq. (29), the stirring efficiency decreases with time as a result of cooling. In the case with weak ppv, τ evolves rapidly toward values close to 15 Myrs and 90 Myrs, for $\Delta\eta_{ppv} = 10^{-4}$ and $\Delta\eta_{ppv} = 10^{-3}$, respectively. The time evolution of τ for cases with neutral and strong ppv is more gradual, reaching values of mixing times at about 1100 Myrs and 1280 Myrs, respectively. Throughout most of their histories, the stirring efficiencies between strong or neutral ppv differ from that of a weak ppv by a factor ~10–100. These orders of magnitude differences in mixing times at final time are comparable or larger to what we measured in our numerical experiments at statistically steady state (Fig. 3).

6. Discussion

Clearly, the numerical experiments and the parameterized thermal evolution coupled to the chaotic mixing model presented here do not account for the diversity of Earth's mantle processes and their complex interactions. It is good to keep in mind that the present study is subject to a number of simplifications.

Our numerical experiments are carried out in 2D Cartesian geometry, using a simple Newtonian rheology with a relatively small sensitivity of viscosity to temperature, and pure basal heating. However, the influence of ppv strength on mantle thermo-chemical evolution, in spherical geometry with more Earth-like rheology and mixed heating was recently investigated by Nakagawa and Tackley (2011). They concluded that the presence of weak ppv increases the heat flux and mantle temperature and convective velocities, in good agreement with the results of our study. In addition, kinematic models have shown that the presence of toroidal components absent in our 2D numerical experiments could influence the efficiency on stirring processes (Ferrachat and Ricard, 1998). However, as shown in Coltice and Schmalzl (2006) the stirring efficiency in a convecting mantle is a function of the magnitude of convective velocities for both 2D and 3D geometries. Therefore, we expect our main results on the influence of ppv strength on stirring efficiency to hold for 3D convective systems.

Importantly, we have only considered Newtonian rheologies, while the possibility of non-Newtonian ppv is suggested by experimental work (Ammann et al., 2010). Using 2D numerical experiments, Ten et al. (1997) have concluded that non-Newtonian convective mixing is slower than Newtonian convective mixing in a similar context (*i.e.*, with comparable heat fluxes and velocities). Although in these experiments the non-Newtonian regions spanned the whole convective domain instead of a smaller area (as in the models presented in this manuscript), the influence of strain-rate dependent rheology could play a role, which remains to be investigated dynamically.

Although our predicted value of mixing times (*e.g.*, Fig. 3) are not definitive, the magnitude of the differences between the cases with distinct ppv strengths appears to be a robust diagnostic.

Nevertheless, additional investigations should be carried out in the future, in order to better quantify the impact of ppv on Earth's thermal and chemical history. In particular, the development of more accurate scaling laws to characterize the thermal evolution of a convective system in the presence of ppv needs to be performed, by carrying out a systematic exploration of the parameter space, such as the value of the Rayleigh numbers, the pv–ppv Clapeyron slope and the viscous rheology, including strain-rate dependent viscosity that might be appropriate for the ppv phase (Ammann et al., 2010).

7. Conclusions

We have investigated the influence of post-perovskite strength on Earth's mantle convective dynamics and stirring efficiency, using numerical experiments and simple analytical theory. We show that the viscosity of the post-perovskite phase can have a dramatic influence on mantle convective dynamics: weak post-perovskite enhances the destabilization of the bottom thermal boundary layer, increasing significantly the heat flux. This yields an increase in mantle temperatures that can be predicted, using simple energy scalings. This increase in mantle temperature lowers viscosity, and enhances the convective vigor.

The stirring efficiencies measured in our numerical experiments show a significant increase with decreasing the post-perovskite strength. This observed influence is well reproduced by a simple chaotic mixing model. This indicates that mantle stirring efficiency is related to the change in the magnitude of convective velocities triggered by the presence of post-perovskite with distinct rheology.

By coupling this mixing model with a parameterized convection evolution, we find that the presence of weak post-perovskite can increase mantle convective stirring efficiency by at least one order of magnitude. The influence of a weak post-perovskite on mantle thermal evolution and convective stirring efficiency is maximized if the post-perovskite phase appears early in the mantle thermal history.

Our results suggest that the effect of post-perovskite strength on the thermal and chemical evolution of the Earth mantle must be accounted for when interpreting surface observations such as heat flow measurements and the geochemical record.

Acknowledgments

We thank Masaki Yoshida and two anonymous reviewers for their thoughtful suggestions, which improved our manuscript. Henri Samuel acknowledges the funds from the *Stifterverband für die Deutsche Wissenchaft*. Nicola Tosi acknowledges support from the Czech Science Foundation (project P2/11/1366), the Deutsche Forschungs Gemeinschaft (grant TO 704/1-1), and the Helmholtz Gesellschaft through the research Alliance "Planetary Evolution and Life". Figures were made with the Generic Mapping Tools (P. Wessel and W.H.F Smith, EOS, Trans. AGU 76 (1995) 329).

References

Ammann, M.W., Brodholt, J.P., Wookey, J., Dobson, D.P., 2010. First-principles constraints on diffusion in lower-mantle minerals and a weak D″ layer. Nature 465, 462–465.
Batchelor, G.K., 1967. An Introduction to Fluid Dynamics. Cambridge University Press, Cambridge.
Boffa Ballaran, T., Trønnes, R.G., Frost, D., 2007. Equations of state of $CaIrO_3$ perovskite and post-perovskite phases. Am. Mineral. 92, 1760–1763.
Buffet, B.A., 2007. A bound on heat flow below a double crossing of the perovskite–postperovskite phase transition. Geophys. Res. Lett. 34. doi:10.1029/2007GL030930.
Chandrasekhar, S., 1961. Hydrodynamic and Hydromagnetic Stability. Dover, New York, USA.
Cheng, J.-G., Zhou, J.-S., Goodenough, J.N., Sui, Y., Ren, Y., Suchomel, M.R., 2011. High-pressure synthesis and physical properties of perovskite and post-perovskite $Ca_{1-x}Sr_xIrO_3$. Phys. Rev. B 83.
Chopelas, A., Boehler, R., 1992. Thermal expansivity in the lower mantle. J. Geophys. Res. 19, 1983–1986.
Christensen, U.R., Hofmann, A.W., 1994. Segregation of subducted oceanic crust in the convecting mantle. J. Geophys. Res. 99, 19,867–19,884.
Christensen, U.R., Yuen, D.A., 1985. Layered convection induced by phase transitions. J. Geophys. Res. 90, 10291–10300.
Čižkovà, H., Čadek, O., Matyska, C., Yuen, D.A., 2010. Implications of post-perovskite transport properties for core–mantle dynamics. Phys. Earth Planet. Inter. 180, 235–243.
Coltice, N., 2005. The role of convective mixing in degassing the Earth's mantle. Earth Planet. Sci. Lett. 234 (1–2), 15–25.
Coltice, N., Schmalzl, J., 2006. Mixing times in the mantle of the early Earth derived from 2-D and 3-D numerical simulations of convection. Geophys. Res. Lett. 33 (23). doi:10.1029/2006GL027707.
Conrad, C.P., Hager, B.H., 1999. Effect of plate bending and fault strength at subduction zone on plate dynamics. J. Geophys. Res. 104, 17551–17571.
Davies, G.F., 1980. Thermal histories of convective Earth models and constraints on radiogenic heat production in the Earth. J. Geophys. Res. 85, 2517–2530.
Farnetani, C.G., Samuel, H., 2003. Lagrangian structures and stirring in the Earth's mantle. Earth Planet. Sci. Lett. 206, 335–348.
Ferrachat, S., Ricard, Y., 1998. Regular vs. chaotic mantle mixing. Earth Planet. Sci. Lett. 155, 75–86.
Ferrachat, S., Ricard, Y., 2001. Mixing properties in the Earth's mantle: effects of the viscosity stratification and of oceanic crust segregation. Geochem. Geophys. Geosyst. doi:2000GC000092.
Forte, A.M., Mitrovica, J.X., 2001. Deep-mantle high-viscosity flow and thermochemical structure inferred from seismic and geodynamic data. Nature 410, 1049–1056.
Guignot, N., Andrault, D., Morad, G., Bolfan-Casanova, N., Mezouar, M., 2007. Thermoelastic properties of post-perovskite phase $MgSiO_3$ determined experimentally at core–mantle boundary P–T conditions. Earth Planet. Sci. Lett. 256, 162–168.
Hernlund, J.W., Thomas, C., Tackley, P.J., 2005. A doubling of the post-perovskite phase boundary and structure of the Earth's lowermost mantle. Nature 434, 882–886.
Hirose, K., Karato, S.-i., Cormier, V.F., Brodholt, J.P., Yuen, D.A., 2006. Postperovskite phase transition and its geophysical implications. Rev. Geophys. 44. doi:10.1029/2005RG000186.
Hoffman, N.R.A., McKenzie, D.P., 1985. The destruction of geochemical heterogeneities by differential fluid motions during mantle convection. Geophys. J. R. Astron. Soc. 82, 163–206.
Hunt, D.L., Kellogg, L.H., 2001. Mixing and development of heterogeneities in the mantle: the role of depth-dependent viscosity. J. Geophys. Res. 106, 6747–6759.
Hunt, S.A., Weidner, D.J., Li, L., Wang, L.P., Walte, N.P., Brodholt, J.P., Dobson, D.P., 2009. Weakening of calcium iridate during its transformation from perovskite to post-perovskite. Nat. Geosci. 11, 794–797.
Ito, I., Toriumi, M., 2010. Silicon self-diffusion of $MgSiO_3$ perovskite by molecular dynamics and its implication for lower mantle rheology. J. Geophys. Res. 115 (B12205). doi:10.1029/2010JB000843.
Jaupart, C., Mareschal, J.-C., 2011. Heat Generation and Transport in the Earth. Cambridge Univ Press.
Karato, S.-I., 2011. Rheological structure of the mantle of a super-Earth: some insights from mineral physics. Icarus 212, 14–23.
Katsura, T., Yokoshi, S., Kawabe, K., Shatskiy, A., Manthilake, M.A.G.M., Zhai, S., Fukui, H., Hegoda, H.A.C.I., Yoshino, T., Yamazaki, D., Matsuzaki, T., Yoneda, A., Ito, E., Sugita, M., Tomioka, N., Hagiya, K., Nozawa, A., Funakoshi, K., 2009. P–V–T relations of $MgSiO_3$ perovskite determined by in situ X-ray diffraction using a large-volume high-pressure apparatus. Geophys. Res. Lett. 36 (L01305). doi:10.1029/2008GL035658.
King, S.D., Lee, C., van Keken, P., Leng, W., Zhong, S., Tan, E., Tosi, N., Kameyama, M., 2010. A community benchmark for 2D Cartesian compressible convection in the Earth's mantle. Geophys. J. Int. 180, 73–87.
Komabayashi, T., Hirose, K., Sugimura, E., Sata, N., Ohishi, Y., Dubrovinsky, L., 2008. Simultaneous volume measurements of post-perovskite and perovskite in $MgSiO_3$ and their thermal equations of state. Earth Planet. Sci. Lett. 265, 515–524.
Lay, T., Hernlund, J.W., Garnero, E.J., Thorne, M.S., 2006. A post-perovskite lens and D″ heat flux beneath the central Pacific. Science 314, 1272–1276.
Manga, M., 1996. Mixing of chemical heterogeneities in the mantle: effect of viscosity differences. Geophys. Res. Lett. 23, 403–406.
Matyska, C., Yuen, D.A., 2006. Lower mantle dynamics with the post-perovskite phase change, radiative thermal conductivity, temperature- and depth-dependent viscosity. Phys. Earth Planet. Inter. 154, 196–207.
Merveilleux du Vignaux, N., Fleitout, L., 2002. Stretching and mixing of viscous blobs in the Earth's mantle. J. Geophys. Res. 106, 30,893–30,908.
Monnereau, M., Yuen, D.A., 2007. Topology of the postperovskite phase transition and mantle dynamics. Proc. Natl. Acad. Sci. 104, 9156–9161.
Monnereau, M., Yuen, D.A., 2010. Seismic imaging of the D″ and constraints on the core heat flux. Phys. Earth Planet. Inter. 180, 258–270.
Murakami, M., Hirose, K., Kawamura, K., Sata, N., Ohishi, Y., 2004. Post-perovskite phase transition in $MgSiO_3$. Science 304, 855–858.
Nakagawa, T., Tackley, P.J., 2004. Effects of a perovskite–post perovskite phase change near core–mantle boundary in compressible mantle convection. Geophys. Res. Lett. 31. doi:10.1029/2004GL020648.
Nakagawa, T., Tackley, P.J., 2006. Three-dimensional structures and dynamics in the deep mantle: effects of post-perovskite phase change and deep mantle layering. Geophys. Res. Lett. 33. doi:10.1029/2006GL025719.
Nakagawa, T., Tackley, P.J., 2011. Effects of low-viscosity post-perovskite on thermo-chemical mantle convection in a 3-D spherical shell. Geophys. Res. Lett. 38. doi:10.1029/2010GL046494.
Naliboff, J.B., Kellogg, L.H., 2006. Dynamic effects of a step-wise increase in thermal conductivity and viscosity in the lowermost mantle. Geophys. Res. Lett. 33, L12S09.
Naliboff, J.B., Kellogg, L.H., 2007. Can large increases in viscosity and thermal conductivity preserve large-scale heterogeneity in the mantle? Phys. Earth Planet. Inter. 161, 86–102.
Oganov, A.R., Ono, S., 2004. Theoretical and experimental evidence for a post-perovskite phase of $MgSiO_3$ in Earth's D″. Nature 430, 445–4448.
Oganov, A.R., Ono, S., 2005. The high pressure phase of alumina and implications for Earth's D″ layer. Proc. Natl. Acad. Sci. 102, 10828–10831.
K. Ohta, Electrical and thermal conductivity of the Earth's lower mantle, Ph.D. thesis, Tokyo Institute of Technology, 2010.
Ottino, J.M., 1989. The Kinematics of Mixing: Stretching, Chaos and Transport. Cambridge University Press, Cambridge.
Ricard, Y., Wuming, B., 1991. Inferring the mantle viscosity and its three dimensional structure from geoid, topography and plate velocities. J. Geophys. Res. 105, 561–571.
Samuel, H., Farnetani, C.G., 2003. Thermochemical convection and helium concentrations in mantle plumes. Earth Planet. Sci. Lett. 207, 39–56.
Samuel, H., Aleksandrov, V., Deo, B., 2011. The effect of continents on mantle convective stirring. Geophys. Res. Lett. 38 (L04307). doi:10.1029/2010GL046056.
Schubert, G., Stevenson, D., Cassen, P., 1980. Whole planet cooling and the radiogenic heat source contents of the Earth and Moon. J. Geophys. Res. 85, 2531–2538.
Solomatov, V.S., 1995. Scaling of temperature- and stress-dependent viscosity convection. Phys. Fluids 7, 266–274.
Solomatov, V.S., Reese, C.C., 2008. Grain size variations in the Earth's mantle and the evolution of primordial chemical heterogeneities. J. Geophys. Res. 113. doi:10.1029/2007JB005319.

Steinberger, B., Calderwood, A.R., 2006. Models of large-scale viscous flow in the Earth's mantle with constraints from mineral physics and surface observations. Geophys. J. Int. 167, 1461–1481.
Steinberger, B., Holme, R., 2008. Mantle flow models with core–mantle boundary constraints and chemical heterogeneities in the lowermost mantle. J. Geophys. Res. 113 (B05403). doi:10.1029/2007JB005080.
Tackley, P.J., 2007. Mantle geochemical geodynamics. In: Schubert, G., Bercovici, D. (Eds.), Treatise on Geophysics, vol. 7. Elsevier, pp. 437–505.
Tateno, S., Hirose, K., Sata, N., Ohishi, Y., 2009. Determination of post-perovskite phase transition boundary up to 4400 K and implications for thermal structure in D″ layer. Earth Planet. Sci. Lett. 277, 130–136.
Ten, A., Yuen, D.A., Podladchikov, Y.Y., Larsen, T.B., Pachepsky, E., Malevsky, A.V., 1997. Fractal features in mixing of non-Newtonian and Newtonian mantle convection. Earth Planet. Sci. Lett. 146 (3–4), 401–414.
Tosi, N., Čadek, O., Martinec, Z., Yuen, D.A., Kaufmann, G., 2009. Is the long-wavelength geoid sensitive to the presence of post-perovskite above the core–mantle boundary? Geophys. Res. Lett. 36. doi:10.1029/2008GL036902.
Tosi, N., Yuen, D.A., Čadek, O., 2010. Dynamical consequences in the lower mantle with the post-perovskite phase change and strongly depth-dependent thermodynamic and transport properties. Earth Planet. Sci. Lett. 298, 229–243.
van der Hilst, R.D., de Hoop, M., Wang, P., Shim, S.-H., Tenorio, L., 2007. Seismostratigraphy and thermal structure of Earth's core–mantle boundary region. Science 315, 1813–1817.
van Keken, P.E., Ballentine, C.J., 1998. Whole mantle versus layered mantle convection and the role of a high-viscosity lower mantle in terrestrial volatile evolution. Earth Planet. Sci. Lett. 109, 129–150.
van Keken, P.E., Ballentine, C.J., Hauri, E., 2003. Convective mixing in the Earth's mantle. In: Turekian, Holland (Ed.), Geochemistry of the Mantle and Core. Elsevier.